# A Trajectory-Driven 3D Channel Model for Human Activity Recognition

**AHMED ABDELGAWWAD**[1], **ANDREU CATALÀ MALLOFRÉ**[2],
**AND MATTHIAS PÄTZOLD**[1], (Senior Member, IEEE)

[1]Faculty of Engineering and Science, University of Agder, 4898 Grimstad, Norway
[2]Technical Research Centre for Dependency Care and Autonomous Living (CETpD), Universitat Politècnica de Catalunya (UPC), Vilanova i la Geltrú, 08800 Barcelona, Spain

Corresponding author: Ahmed Abdelgawwad (ahmed.abdel-gawwad@uia.no)

**ABSTRACT** This paper concerns the design, analysis, and simulation of a 3D non-stationary channel model fed with inertial measurement unit (IMU) data. The work in this paper provides a framework for simulating the micro-Doppler signatures of indoor channels for human activity recognition by using radio-frequency-based sensing technologies. The major human body segments, such as wrists, ankles, torso, and head, are modelled as a cluster of moving point scatterers. We provide expressions for the time variant (TV) speed and TV angles of motion based on 3D trajectories of the moving person. Moreover, we present mathematical expressions for the TV Doppler shifts and TV path gains associated with each moving point scatterer. Furthermore, a model of the non-stationary time variant channel transfer function (TV-CTF) is provided, which takes into account the effects caused by a moving person as well as fixed objects, such as furniture, walls, and ceiling. The micro-Doppler signatures of the moving person is extracted from the TV-CTF by employing the concept of the spectrogram, whose expression is also provided in closed form. Our model is confirmed by channel state information (CSI) measurements taken during walking, falling, and sitting activities. The proposed channel model is fed with IMU data that has been collected. We evaluate the micro-Doppler signature of the model and CSI measurements. The results show a good agreement between the spectrograms and the TV mean Doppler shifts of our IMU-driven channel model and the measured CSI. The proposed model enables a paradigm shift from traditional experimental-based approaches to future simulation-based approaches for the design of human activity recognition systems.

**INDEX TERMS** Human activity recognition, non-stationary fading channels, channel state information, channel transfer function, spectrogram, time-variant Doppler power characteristics, micro-Doppler signature, channel measurements, inertial measurement units, Internet of Things, wireless sensing.

## I. INTRODUCTION

The unsupervised monitoring of human mobility parameters during the activities of daily living is generating a high interest in the medical community, especially after the explicit recommendation of the US Food and Drug Administration [1] and the European Medicines Agency [2] that it is desirable to include information from portable or context-aware systems in clinical trials. Other reasons for the high interest are the increase of fall incidents among adults over 65 years

The associate editor coordinating the review of this manuscript and approving it for publication was Donato Impedovo.

according to the US fall report [3] and the high mortality rate caused by fall incidents according to the World Population Ageing Report of the United Nations [4]. Although there are still many problems to solve, mainly in the lack of gold standards, a good indication of the growth prospect of these context-aware systems is their adoption and development in the next five years by the main pharmaceutical companies of the diseases related to pathological human movement [5]. Monitoring systems can detect movement disorders, which can be signs of physical and mental illness and fragility. Small changes in the quality and complexity of movements can be indicators of an impending deterioration in health

status, which in many cases can be reversed with appropriate rehabilitation measures.

The first challenge in the development of monitoring systems is to clearly identify the main types of movements used in clinical practice, such as cadence when walking, stride length, sit to stand, stand to sit, turns, and adverse events such as falls. The accurate and convenient measurement of the above parameters at the user's home over long periods of time is a milestone that may lead to significant advances in geriatrics.

This article is part of a recent line of research that tries to extract knowledge from human activities at home using conventional Wi-Fi systems. Such systems have the advantages over wearable systems as they are easy to use, comfortable, have low cost, no stigmatization, and universal availability. The enormous penetration of Wi-Fi systems in all households carries a high degree of acceptance. In addition, such systems do not violate the users' privacy like human activity recognition (HAR) systems based on camera surveillance [6]–[9]. Moreover, they do not require user involvement, which is mandatory when using smartphones or wearable sensors [10]–[13] that may be forgotten to wear. With Wi-Fi systems, it is possible to collect radio-frequency (RF) sensing data continuously while the users can carry out their daily living activities without disturbance.

The literature describes radar systems for classifying human activities [14]–[19], such as arm motion recognition for human-computer interaction in smart homes [20], gesture recognition [21]–[23], differentiation of unarmed and armed people for security services [24], and the detection of gait asymmetries [25], [26]. In all these mentioned applications the spectrogram was employed. The spectrogram is a quadratic time-frequency power distribution that provides insight into the micro-Doppler signature of non-stationary multicomponent signals influenced by human activities.

A tool for capturing the complex channel state information (CSI) has been developed by the authors of [27]. Such a tool enables the collection of RF data over 30 subcarriers and operates according to the IEEE 802.11n standard [28]. Laptops equipped with the NIC 5300 wireless network module are able to run this tool. The authors of [29] provided a survey on many contributions of different activity recognition systems by analyzing the amplitude of the CSI data acquired by the NIC 5300 module. The main drawback of the CSI tool is that the phases of the data collected are highly distorted. This is due to the clock asynchronization between the transmitter and receiver stations which makes it challenging to analyze the micro-Doppler signatures of the collected CSI data. If the spectrogram of the measured CSI is very noisy, it does not provide a clear insight into the time variant (TV) Doppler power characteristics. For noise supression, the principle component analysis [30] was applied to the amplitudes of measured CSI data, and then the one-sided spectrogram was computed. An alternative approach is to apply a linear transformation to the highly distorted phases to eliminate the phase distortions [31]. Although this approach

succeeds in providing a good pattern of the transformed phases, it can partially eliminate the desired phases, which might limit the insight into the true micro-Doppler signature. A reliable solution to eliminate the phase distortions is to employ a physical back-to-back (B2B) connection. This approach was introduced, implemented, tested, and verified in [32].

The main disadvantage of the systems based on RF sensing in [14]–[22], [24]–[26] is that they require measurement data to train the classifier. This consumes a huge amount of time and effort to collect non-reproducible data. An alternative approach is to generate simulation-based reproducible data to train the classifier. In the literature, many attempts have been done to simulate radar micro-Doppler signatures of human activities such as walking in [33], [34]. The authors of [35] have provided a framework to estimate the gait parameters from simulated radar micro-Doppler signatures of human walking activity, where the Thalmann human walking model described in [36] has been incorporated. motion capture (MOCAP) databases have been employed in [37] to simulate the radar micro-Doppler signatures of different human activities such as crawling, creeping, and running. An alternative approach was to use the Microsoft Kinect sensor for collecting the trajectories to simulate the radar micro-Doppler signatures of human activities, such as walking, running, leaping, and boxing in [38].

To the best of our knowledge, inertial measurement units (IMUs) have not been used to simulate the micro-Doppler signatures of CSI channel models under the influence of human activities. The trajectories of the moving body segments can be measured by attaching the IMUs to the moving body segments. The IMUs collect the accelerations and the Euler angles. Then, we rotate the accelerations to get their projections on the reference frame. Finally, the trajectories computed from the rotated accelerations can be fed to the channel model. Such an IMU-driven channel model enables to simulate the micro-Doppler signatures.

In this paper, we present an IMU-driven non-stationary channel model that enables to simulate the multipath components associated with different body segments. Moreover, such a model allows for in-depth understanding of the parameters that have influence on the Doppler shifts caused by the moving body segments. The contributions of this paper are listed as follows

- The moving body segments are modelled as a cluster of moving point scatterers.
- We present expressions of the TV speed, time variant azimuth angle of motion (TV-AAOM), and time variant elevation angle of motion (TV-EAOM) corresponding to each moving point scatterer.
- The expressions of the TV Doppler shift and the TV propagation delay associated with each moving point scatterer are provided.
- The TV path gains of the moving point scatterers are taken into account to make the proposed channel model more realistic.

- We present a model for the time variant channel transfer function (TV-CTF).
- The micro-Doppler signature is extracted from the TV-CTF by means of the spectrogram, of which the closed-form expressions are provided.
- The proposed channel model is confirmed by performing the CSI and IMU measurements simultaneously for human activities.
- The spectrograms of both the CSI measurements and the IMU-driven channel model are evaluated. In addition, the results of the TV mean Doppler shifts (TV-MDSs) computed from the spectrograms are matching.

The contributions of this paper pave the way towards design of the simulation-based HAR systems.

The rest of the paper is organized as follows. Section II describes the 3D multipath propagation scenario and presents the expressions of the TV Doppler shifts, TV path gains, and the non-stationary TV-CTF corresponding to the IMU-driven channel model. Section III presents the expressions of the spectrogram of the TV-CTF. Section IV shows how the CSI and IMU data were collected, addresses the challenges faced while processing the data, and exhibits the results of the proposed IMU-driven channel model and the measured CSI data. Section V is left for the conclusion and provides an outlook to future research.

### List of Abbreviations

| | |
|---|---|
| B2B | back-to-back |
| CSI | channel state information |
| CTF | channel transfer function |
| F2F | fixed-to-fixed |
| HAR | human activity recognition |
| IMU | inertial measurement unit |
| MOCAP | motion capture |
| RF | radio-frequency |
| ST-FT | short-time Fourier transform |
| ST-CTF | short-time CTF |
| TFPD | time-frequency-power distribution |
| TV | time variant |
| TV-EAOA | time variant elevation angle of arrival |
| TV-EAOD | time variant elevation angle of departure |
| TV-AAOA | time variant azimuth angle of arrival |
| TV-AAOD | time variant azimuth angle of departure |
| TV-MDS | TV mean Doppler shift |
| TV-EAOM | time variant elevation angle of motion |
| TV-AAOM | time variant azimuth angle of motion |
| TV-CTF | time variant channel transfer function |
| ZUPT | zero-update |

## II. MODELLING THE TV-CTF
### A. THE GEOMETRICAL MODEL

In this paper, we consider an indoor propagation scenario described by the geometrical model in Fig. 1. The geometrical model includes a Wi-Fi transmitter and a Wi-Fi receiver denoted by $T_x$ and $R_x$, respectively. Both $T_x$ and $R_x$ are stationary and located at $\left(x^T, y^T, z^T\right)$ and $\left(x^R, y^R, z^R\right)$,
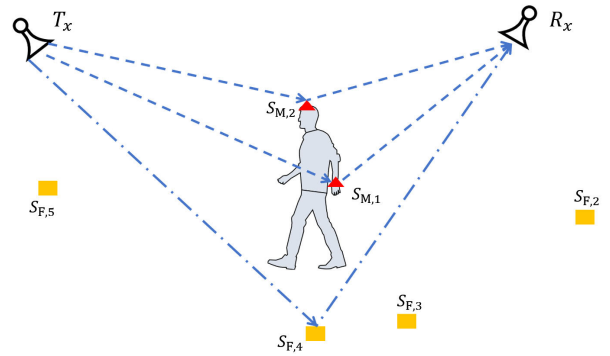


**FIGURE 1.** Geometrical model of an indoor propagation scenario with a fixed transmitter $T_x$, a fixed receiver $R_x$, a moving person modelled by moving point scatterers (▲), and several fixed scatterers (■) representing stationary objects, such as walls, furniture, etc.

respectively, and operate according to the IEEE 802.11n standard [28]. We consider a person performing some activities during which the person's main body segments are modelled by a cluster of $\mathcal{N}$ moving point scatterers $S_{M,n}$ for $n = 1, 2, \ldots, \mathcal{N}$. Moreover, the fixed objects, such as walls, furniture, etc. are modelled as $\mathcal{M}$ fixed scatterers $S_{F,m}$ for $m = 1, 2, \ldots, \mathcal{M}$. Single-bounce scattering is assumed, i.e., any wave transmitted from the $T_x$ reaches the $R_x$ via either a moving point scatterer $S_{M,n}$ or a fixed scatterer $S_{F,m}$. The line-of-sight is assumed to be obstructed.

### B. THE TV TRAJECTORIES
The TV velocity $\vec{v}_{M,n}(t)$ associated with the $n$th moving point scatterer $S_{M,n}$ is presented as

$$\vec{v}_{M,n}(t) = \left[v_{M,n,x}(t), v_{M,n,y}(t), v_{M,n,z}(t)\right]^{\mathrm{T}} \quad (1)$$

where the vector transpose operation is denoted by $[\cdot]^{\mathrm{T}}$. The velocities $v_{M,n,x}(t)$, $v_{M,n,y}(t)$, and $v_{M,n,z}(t)$ in $x$, $y$, and $z$ directions, respectively can be expressed in terms of the TV speed $v_{M,n}(t)$, TV-EAOM $\beta_{v_{M,n}}(t)$ and TV-AAOM $\alpha_{v_{M,n}}(t)$ as

$$v_{M,n,x}(t) = v_{M,n}(t)\cos\left(\beta_{v_{M,n}}(t)\right)\cos\left(\alpha_{v_{M,n}}(t)\right) \quad (2)$$
$$v_{M,n,y}(t) = v_{M,n}(t)\cos\left(\beta_{v_{M,n}}(t)\right)\sin\left(\alpha_{v_{M,n}}(t)\right) \quad (3)$$
$$v_{M,n,z}(t) = v_{M,n}(t)\sin\left(\beta_{v_{M,n}}(t)\right) \quad (4)$$

respectively. The TV functions $\alpha_{v_{M,n}}(t)$ and $\beta_{v_{M,n}}(t)$ are computed by

$$\alpha_{v_{M,n}}(t) = \text{arctan2}\left(v_{M,n,y}(t), v_{M,n,x}(t)\right) \quad (5)$$

$$\beta_{v_{M,n}}(t) = \arcsin\left(\frac{v_{M,n,z}(t)}{\sqrt{v_{M,n,x}^2(t)+v_{M,n,y}^2(t)+v_{M,n,z}^2(t)}}\right) \quad (6)$$

respectively. The elevation angle $\beta_{v_{M,n}}(t)$ described in (6) has a range from $-\pi/2$ to $\pi/2$, i.e., $\beta_{v_{M,n}}(t) \in [-\pi/2, \pi/2]$. The function arctan2($\cdot$) returns an angle with a range from $-\pi$ to $\pi$, i.e., $\alpha_{v_{M,n}}(t) \in [-\pi, \pi)$. From (2)–(4), the TV displacements $x_{M,n}(t)$, $y_{M,n}(t)$, and $z_{M,n}(t)$ can be calculated

as follows

$$x_{M,n}(t) = x_{M,n} + \int_0^t v_{M,x}(t')dt' \qquad (7)$$

$$y_{M,n}(t) = y_{M,n} + \int_0^t v_{M,y}(t')dt' \qquad (8)$$

$$z_{M,n}(t) = z_{M,n} + \int_0^t v_{M,z}(t')dt' \qquad (9)$$

respectively. The parameters $x_{M,n}$, $y_{M,n}$, $z_{M,n}$ designate the initial positions of $S_{M,n}$ in the $x$, $y$, and $z$ directions, respectively. By using the TV displacements in (7)–(9) and the location of $T_x$, the TV Euclidean distance $d_{M,n}^T(t)$ between the $n$th moving point scatterer $S_{M,n}$ and the transmitter $T_x$ is given by

$$d_{M,n}^T(t) = \left( \left( x_{M,n}(t) - x^T \right)^2 + \left( y_{M,n}(t) - y^T \right)^2 \right.$$
$$\left. + \left( z_{M,n}(t) - z^T \right)^2 \right)^{\frac{1}{2}}. \qquad (10)$$

Similarly, the TV Euclidean distance $d_{M,n}^R(t)$ between the $n$th moving point scatterer $S_{M,n}$ and the receiver $R_x$ can be expressed by

$$d_{M,n}^R(t) = \left( \left( x_{M,n}(t) - x^R \right)^2 + \left( y_{M,n}(t) - y^R \right)^2 \right.$$
$$\left. + \left( z_{M,n}(t) - z^R \right)^2 \right)^{\frac{1}{2}}. \qquad (11)$$

By using the expressions in (7)–(11), the time variant azimuth angle of departure (TV-AAOD) $\alpha_{M,n}^T(t)$, time variant azimuth angle of arrival (TV-AAOA) $\alpha_{M,n}^R(t)$, time variant elevation angle of departure (TV-EAOD) $\beta_{M,n}^T(t)$, and time variant elevation angle of arrival (TV-EAOA) $\beta_{M,n}^R(t)$ can be expressed by

$$\alpha_{M,n}^T(t) = \arctan2\left( y_{M,n}(t) - y^T, \ x_{M,n}(t) - x^T \right) \quad (12)$$

$$\alpha_{M,n}^R(t) = \arctan2\left( y_{M,n}(t) - y^R, \ x_{M,n}(t) - x^R \right) \quad (13)$$

$$\beta_{M,n}^T(t) = \arcsin\left( \frac{z_{M,n}(t) - z^T}{d_{M,n}^T(t)} \right) \qquad (14)$$

$$\beta_{M,n}^R(t) = \arcsin\left( \frac{z_{M,n}(t) - z^R}{d_{M,n}^R(t)} \right) \qquad (15)$$

respectively. The TV functions in (12)–(15) are playing an essential role in providing an expression for the Doppler frequency caused by the $n$th moving point scatterer, which will be discussed later in this section. The TV propagation delay $\tau_{M,n}(t)$ of the wave transmitted by $T_x$ via the $n$th moving point scatterer $S_{M,n}$ and arriving at the receiver $R_x$ can be computed by

$$\tau_{M,n}(t) = \frac{d_{M,n}^T(t) + d_{M,n}^R(t)}{c_0} \qquad (16)$$

where the parameter $c_0$ denotes the speed of light.

## C. THE TV MODEL PARAMETERS

Using the relationship $f_{n,q}(t) = -(f_0+f_q)\dot{\tau}_{M,n}(t)$ in [39], [40], the TV Doppler shift $f_{n,q}(t)$ caused by the $n$th moving point scatterer $S_{M,n}$ and associated with the $q$th subcarrier index can be computed by

$$f_{n,q}(t) = -f_{n,q,\max}(t)\gamma_n(t) \qquad (17)$$

where the function $f_{n,q,\max}(t)$ denotes the maximum Doppler shift caused by the speed of motion of the $n$th moving point scatterer $S_{M,n}$. It is given by

$$f_{n,q,\max}(t) = \frac{(f_0 + f_q)\, v_{M,n}(t)}{c_0} \qquad (18)$$

where the parameter $f_0$ denotes the carrier frequency. The parameter $f_q$ is the $q$th subcarrier frequency, which is given by

$$f_q = q \cdot \Delta f. \qquad (19)$$

The parameter $q \in \{ -28, -26, \ldots, -2, -1, 1, 3, \ldots, 27, 28 \}$ in the expression above designates the subcarrier frequency index in OFDM communication systems that follow the IEEE 802.11n standard [28]. The parameter $\Delta f$ has a constant value of 312.5 kHz.

The function $\gamma_n(t)$ in (17) is calculated by

$$\gamma_n(t)$$
$$= \cos\left( \beta_{v_{M,n}}(t) \right) \left[ \cos\left( \beta_{M,n}^T(t) \right) \cos\left( \alpha_{M,n}^T(t) - \alpha_{v_{M,n}}(t) \right) \right.$$
$$\left. + \cos\left( \beta_{M,n}^R(t) \right) \cos\left( \alpha_{v_{M,n}}(t) - \alpha_{M,n}^R(t) \right) \right]$$
$$+ \sin\left( \beta_{v_{M,n}}(t) \right) \left[ \sin\left( \beta_{M,n}^T(t) \right) + \sin\left( \beta_{M,n}^R(t) \right) \right]. \quad (20)$$

The TV function described by (20) is a combination of the trigonometric functions of the TV-AAOD $\alpha_{M,n}^T(t)$, time variant azimuth angle of arrival (TV-AAOA) $\alpha_{M,n}^R(t)$, TV-EAOD $\beta_{M,n}^T(t)$, TV-EAOA $\beta_{M,n}^R(t)$, TV-EAOM $\beta_{v_{M,n}}(t)$, and TV-AAOM $\alpha_{v_{M,n}}(t)$. Thus, it depends on the direction of motion and location of the moving point scatterer $S_{M,n}$ and the fixed locations of the $T_x$ and $R_x$. Note that the function $\gamma_n(t)$ can have either positive or negative values and scales the maximum Doppler shift $f_{n,q,\max}(t)$. If the moving point scatterer $S_{M,n}$ moves towards the $T_x$ and $R_x$, the propagation delay $\tau_{M,n}(t)$ decreases, and its rate of change $\dot{\tau}_{M,n}(t)$ is negative. Thus, from (17) it follows that the function $\gamma_n(t)$ is negative and the Doppler frequency $f_{n,q}(t)$ has positive values according to (17). When $S_{M,n}$ moves away from the $T_x$ and $R_x$, the propagation delay $\tau_{M,n}(t)$ increases, and the rate of change $\dot{\tau}_{M,n}(t)$ has positive values. Hence, the function $\gamma_n(t)$ is positive and the TV Doppler frequency $f_{n,q}(t)$ becomes negative. This shows how strongly the locations of the moving point scatterer $S_{M,n}$, $T_x$, and $R_x$ influence the values of the TV Doppler frequency $f_{n,q}(t)$. Thus, by changing the locations of the $T_x$ and $R_x$, we will have different values of the Doppler frequency $f_{n,q}(t)$. Note that the Doppler frequency $f_{n,q}(t)$ in (17) is assumed to be linear function of time over short time intervals. A special case occurs when the $T_x$ and $R_x$

are co-located, e.g., as in a mono-static radar configuration, then the TV functions $\alpha_{M,n}^T(t)$ and $\beta_{M,n}^T(t)$ become equivalent to $\alpha_{M,n}^R(t)$ and $\beta_{M,n}^R(t)$, respectively. Hence, the expression for $\gamma_n(t)$ reduces to

$$\gamma_n(t) = 2 \times \Big[ \cos\left(\beta_{v_{M,n}}(t)\right) \cos\left(\beta_{M,n}^T(t)\right)$$
$$\times \cos\left(\alpha_{M,n}^T(t) - \alpha_{v_{M,n}}(t)\right)$$
$$+ \sin\left(\beta_{v_{M,n}}(t)\right) \sin\left(\beta_{M,n}^T(t)\right) \Big]. \quad (21)$$

Note that if the subcarrier frequency $f_q$ is much smaller than the values of the carrier frequency $f_0$, i.e., $f_q \ll f_0$, the influence of the subcarrier frequency $f_q$ on the Doppler frequency is much smaller than that of the carrier frequency $f_0$. Thus, the Doppler frequency of the moving point scatterer $S_{M,n}$ is the same for all the subcarrier frequencies, i.e., $f_{n,q}(t) \approx f_{n,p}(t)$ for $p \neq q$.

The TV path gain $c_{M,n}(t)$ associated with the $n$th moving point scatterer $S_{M,n}$ is expressed by [41], [42]

$$c_{M,n}(t) = \lambda\, a_{M,n} \left[ d_{M,n}^R(t)\, d_{M,n}^T(t) \right]^{-\frac{\eta}{2}}. \quad (22)$$

The TV path gain $c_{M,n}(t)$ depends on the distances $d_{M,n}^R(t)$ and $d_{M,n}^T(t)$, the wavelength $\lambda = c_0/f_0$, the transmit and receive antenna gains and the contribution of the $n$th moving point scatterer $a_{M,n}$ [43], and the path loss exponent $\eta$. Note that the TV path gain $c_{M,n}(t)$ in (22) does not change quickly with respect to time. Hence, it can be assumed that the path gain $c_{M,n}(t)$ is constant over short-time intervals. The parameters $a_{M,n}$ in (22) is given by

$$a_{M,n} = \sqrt{P_{T_x} G_{T_x} P_{R_x} G_{R_x} A_{M,n}} \quad (23)$$

for $n = 1, 2, \ldots, \mathcal{N}$, where the symbols $P_{T_x}$, $G_{T_x}$, $P_{R_x}$, $G_{R_x}$, and $A_{M,n}$ designate the transmit power, gain of the $T_x$ antenna, receive power, gain of the $R_x$ antenna, and the radar cross-section of the $n$th moving point scatterer $S_{M,m}$, respectively. These parameters are unknown. A method for estimating the parameters $a_{M,n}$ by using the TV-MDS will be demonstrated in Section IV-B.

### D. THE CTF
The TV-CTF $H(t, f_q)$ is given by

$$H(t, f_q) = \sum_{n=1}^{\mathcal{N}} H_{M,n}(t, f_q) + \sum_{m=1}^{\mathcal{M}} H_{F,m} \quad (24)$$

where the first term in (24) denotes the superposition of $\mathcal{N}$ components corresponding to the moving point scatterers. The second term designates the superposition of the $\mathcal{M}$ components corresponding to the fixed scatterers. The components of the first and the second term in (24) are given by

$$H_{M,n}(t, f_q) = c_{M,n}(t)\, e^{j[\theta_{M,n} - 2\pi(f_0 + f_q)\tau_{M,n}(t)]} \quad (25)$$
$$H_{F,m} = c_{F,m}\, e^{j\theta_{F,m}} \quad (26)$$

respectively. The TV-CTF $H_{M,n}(t, f_q)$ in (25) is characterized by a TV path gain $c_{M,n}(t)$, TV propagation delay $\tau_{M,n}(t)$, and phase shift $\theta_{M,n}$ corresponding to the $n$th moving point scatterer $S_{M,n}$.

The expression in (26) is the TV-CTF associated with the $m$th fixed point scatterer $S_{F,m}$ characterized by a constant path gain $c_{F,m}$ and phase shift $\theta_{F,m}$. The phases $\theta_{M,n}$ and $\theta_{F,m}$ are assumed to be identically and independently distributed (i.i.d.), random variables that follow a uniform distribution between $-\pi$ and $\pi$, i.e., $\theta_{M,n}, \theta_{F,m}\, \mathcal{U}(-\pi, \pi]$ [44, p. 36]. The model presented in (24) corresponds to the class of 3D non-stationary fixed-to-fixed (F2F) wideband channels.

The TV-MDS $B_{f_q}(t)$ of the proposed trajectory-driven channel can be expressed in terms of $c_{M,n}(t)$, $c_{F,m}$, and $f_{n,q}(t)$ as

$$B_{f_q}(t) = \frac{\sum_{n=1}^{\mathcal{N}} c_{M,n}^2(t) f_{n,q}(t)}{\sum_{n=1}^{\mathcal{N}} c_{M,n}^2(t) + \sum_{m=1}^{\mathcal{M}} c_{F,m}^2}. \quad (27)$$

The expression above represents the first-order spectral moment, which provides insight into the average Doppler shift caused by the moving point scatterers in the model. This quantity is the sum of the Doppler shifts $f_{n,q}(t)$ weighted by their squared TV path gains $c_{M,n}^2(t)$ and divided by the total sum of the squared path gains of the fixed and moving point scatterers $c_{F,m}^2$ and $c_{M,n}^2(t)$, respectively. The fixed scatterers $S_{F,m}$ do not have any influence on the numerator in (27), as the Doppler shifts caused by the fixed scatterers in F2F channels are zero. On the other hand, their squared path gains $c_{F,m}^2$ influence the denominator in (27). Hence, high values of the path gains $c_{F,m}$ result in small values of the TV-MDS $B_{f_q}(t)$. The expression in (27) can be evaluated by simulations, but not by measurements. That is due to the fact that the values of $f_{n,q}(t)$, $c_{F,m}$, and $c_{M,n}(t)$ are not accessible in the measurement data. An alternative approach for estimating the TV-MDS of CSI measurements by using the spectrogram is presented in the next section.

### III. MICRO-DOPPLER SIGNATURE OF THE TV-CTF
To study the micro-Doppler signature of the non-stationary TV-CTF presented in Section II-D, a time-frequency-power distribution (TFPD) is employed. There are different TFPDs according to the literature [45]–[47]. In this section we use the spectrogram that requires an even, real, and positive window $w(t)$ with normalized energy for computation. In this paper, we utilize a Gaussian window function defined as

$$w(t) = \frac{1}{\sqrt{\sigma_w \sqrt{\pi}}} e^{-\frac{t^2}{2\sigma_w^2}} \quad (28)$$

where the parameter $\sigma_w$ denotes the Gaussian window spread. There are three steps to calculate the spectrogram of the TV-CTF $H(t, f_q)$. First, the TV-CTF $H(t', f_q)$ is multiplied with the sliding window function $w(t' - t)$ to obtain the short-time CTF (ST-CTF) $x_q(t', t)$ according

to [47, Eq. (2.3.1)] as

$$x_q(t', t) = H\left(t' + t, f_q\right) w\left(t'\right). \tag{29}$$

Here, the parameters $t$ and $t'$ denote the local time at which we investigate the micro-Doppler signature and the running time, respectively. The next step is to compute the short-time Fourier transform (ST-FT) $X_q(f, t)$ associated with the $q$th subcarrier by computing the Fourier transform of the ST-CTF $x_q(t', t)$ in (29) as follows

$$X_q(f, t) = \int_{-\infty}^{\infty} x_q(t', t) e^{-j2\pi f t'} dt'$$

$$\approx \frac{e^{-j2\pi ft}}{\sqrt{\sigma_w}\sqrt{\pi}} \left\{ \sum_{n=1}^{\mathcal{N}} X_{M,n,q}(f, t) + \sum_{m=1}^{\mathcal{M}} X_{F,m} \right\} \tag{30}$$

where

$$X_{M,n,q}(f, t) \approx \quad H_{M,n}\left(t, f_q\right) G\left(f, f_{n,q}(t), \sigma_{x,n,q,M}^2\right) \tag{31}$$

$$X_{F,m} = H_{F,m} G\left(f, 0, \sigma_{x,F}^2\right) \tag{32}$$

$$G\left(f, \mu, \sigma^2\right) = \frac{1}{\sqrt{2\pi}\sigma} e^{-\frac{(f-\mu)^2}{2\sigma^2}} \tag{33}$$

$$\sigma_{x,n,q,M}^2 = \frac{1 - j2\pi\sigma_w^2 k_{n,q}}{(2\pi\sigma_w)^2} \tag{34}$$

$$\sigma_{x,F}^2 = \frac{1}{(2\pi\sigma_w)^2} \tag{35}$$

$$k_{n,q} = \frac{df_{n,q}(t)}{dt}. \tag{36}$$

The expression in (30) consists of two terms. The first term designates the superposition of ST-FTs of $\mathcal{N}$ components corresponding to the moving point scatterers. Each component of the first term in (30) is associated with the $n$th moving point scatterer $S_{M,n}$. An approximate solution of each component of the first term is provided in (31), which has been obtained by assuming that the path gains $c_{M,n}(t)$ are constant and the Doppler frequencies $f_{n,q}(t)$ are linear functions of time $t$, over the window function for each moving point scatterer $S_{M,n}$ as mentioned in Section II-D. The function $G(\cdot)$ denotes a Gaussian distribution whose expression is provided in (33). The second term in (30) denotes the superposition of $\mathcal{M}$ components corresponding to the fixed scatterers. Each component of the second term in (32) corresponds to the $m$th fixed scatterer $S_{F,m}$. Note that the ST-FT in (30) is complex valued. The third step is to compute the spectrogram $S_q(f, t)$ associated with the $q$th subcarrier index by taking the magnitude squared of the ST-FT in (30) as

$$S_q(f, t) = |X_q(f, t)|^2 = S_q^{(a)}(f, t) + S_q^{(c)}(f, t). \tag{37}$$

The first term in (37) denotes the auto-term $S_q^{(a)}(f, t)$, whereas the second term is the cross-term $S_q^{(c)}(f, t)$. Note that the spectrogram in (37) is real and positive. The auto-term $S_q^{(a)}(f, t)$ in (37) is real and positive, and its approximation is

given by

$$S_q^{(a)}(f, t) \approx \sum_{n=1}^{\mathcal{N}} \left|X_{M,n,q}(f, t)\right|^2 + \sum_{m=1}^{\mathcal{M}} c_{F,m}^2 G\left(f, 0, \sigma_F^2\right) \tag{38}$$

where [40]

$$\left|X_{M,n,q}(f, t)\right|^2 \approx c_{M,n}^2(t) G\left(f, f_{n,q}(t), \sigma_{n,q,M}^2\right) \tag{39}$$

$$\sigma_{n,q,M}^2 = \frac{1 + \left(2\pi\sigma_w^2 k_{n,q}\right)^2}{2(2\pi\sigma_w)^2} \tag{40}$$

$$\sigma_F^2 = \frac{1}{2(2\pi\sigma_w)^2}. \tag{41}$$

The auto-term in (38) is the superposition of $\mathcal{N} + \mathcal{M}$ components. The first term in (38) denotes the superposition of the auto-terms associated with the $\mathcal{N}$ moving point scatterers. Each component of the first term in (38) contains the desired TV Doppler power characteristics of the $n$th moving point scatterer $S_{M,n}$ associated with the $q$th subcarrier. The expression in (39) represents the approximation of auto-term corresponding to the $n$th moving point scatterer $S_{M,n}$. It is a Gaussian function, which is centered on the Doppler shift $f_{n,q}(t)$, has a variance denoted by $\sigma_{n,q,M}^2$, and is weighted by the squared path gain $c_{M,n}^2(t)$. The second term in (38) denotes the sum of the auto-terms of $\mathcal{M}$ fixed scatterers. Each component of the second term in (38) corresponds to the $m$th fixed scatterer $S_{F,m}$. Moreover, each component of the second term in (38) is a Gaussian function centered on a zero-frequency value as the Doppler frequencies of the fixed scatterers in F2F channels are zero. The Gaussian functions in the second term of (38) are weighted by the squared path gain $c_{F,m}^2$ of the $m$th fixed scatterer $S_{F,m}$. The expression in (38) provides an approximate solution of the power distribution over time and frequency, jointly.

The cross-term $S_q^{(c)}(f, t)$ associated with the $q$th subcarrier is expressed in (43), as shown at the top of the next page. It consists of $(\mathcal{N} + \mathcal{M})(\mathcal{N} + \mathcal{M} - 1)/2$ components. It represents the undesired spectral interference term that reduces the resolution of the spectrogram. This term is real, but not necessarily positive. The operators $\Re\{\cdot\}$ and $\{\cdot\}^*$ in (43) denote the real and complex conjugate operators, respectively. The first term in (43) denotes the sum of the spectral interference components between two moving point scatterers $S_{M,n}$ and $S_{M,i}$ for $n \neq i$. The second term in (43) designates the sum of the spectral interference components between two fixed scatterers $S_{F,m}$ and $S_{F,i}$ for $m \neq i$. Finally, the last term in (43) represents the sum of the spectral interference components between the fixed scatterers $S_{F,m}$ and the moving point scatterers $S_{M,n}$. Averaging the spectrogram $S_q(f, t)$ over the random phases $\theta_{M,n}$ and $\theta_{F,m}$ by simulations removes the cross-term $S_q^{(c)}(f, t)$, i.e., $\mathbf{E}\{S_q(f, t)\}|_{\theta_{M,n}, \theta_{F,m}} = S_q^{(a)}(f, t)$ [48], [49]. In the case of measurements, eliminating the cross-term is still unknown; however, it has been theoretically proven that massive MIMO techniques can help [50].
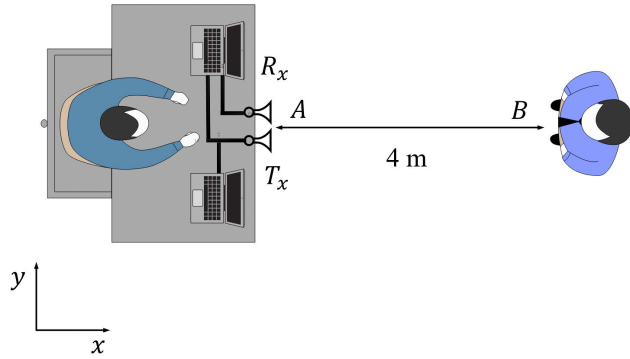
**FIGURE 2.** Measurement scenario in **xy**-plane.

The TV-MDS $B_{H_q}(t)$ can be computed by means of the spectrogram $S_q(f, t)$ as follows

$$B_{H_q}(t) = \frac{\int\limits_{-\infty}^{\infty} f S_q(f, t) df}{\int\limits_{-\infty}^{\infty} S_q(f, t) df}. \tag{42}$$

The expression in (42) can be used in conjunction with simulations and measurements. The numerator of (42) represents the average frequency computed from the spectrogram at each time instant. The numerator in (42) is divided by the total power at each time instant. The TV-MDS $B_{H_q}(t)$ is influenced by the auto-term $S_q^{(a)}(f, t)$ and the cross-term $S_q^{(c)}(f, t)$ in case of measurements; however, it still provides insight into the mean Doppler shifts in the presence of human activities, i.e., $B_{H_q}(t) \approx B_{f_q}(t)$. In the case of simulations, the auto-term $S_q^{(a)}(f, t)$ can be used instead of the spectrogram $S_q(f, t)$ when computing $B_{H_q}(t)$ in (42). Hence, the TV-MDSs $B_{H_q}(t)$ and $B_{f_q}(t)$ become equal [48], i.e., $B_{H_q}(t) \triangleq B_{f_q}(t)$. It is worth mentioning that in the case of measurement data, a notch filter must be used before computing the spectrogram. This is due to the fact that the power spectral density of the signal components associated with the fixed scatterers is much higher than that of moving point scatterers.

## IV. MEASUREMENTS AND NUMERICAL RESULTS

In this section, the TV Doppler power characteristics, the TV-MDSs of the measured RF data and the IMU-driven channel model are presented for some human activities. Moreover, the measurement scenario and the processing of the RF and IMU data are discussed.

### A. MEASUREMENT SCENARIO

Fig. 2 shows the measurement scenario setup in the *xy*-plane. For RF recording, we used a CSI software tool described in [27], [51] and installed it on two HP Elitebooks 6930p laptops. Both laptops had Intel NIC 5300 network adapters and Ubuntu 14.04 LTS operating systems. One laptop was operating in injector mode as $T_x$ while the other was operating in monitor mode as $R_x$. The laptops were connected to a pair of Laird™ YE572113-30SMAM horn antennas. One was a

**TABLE 1.** Initial positions $(x_{\mathrm{M},n}, y_{\mathrm{M},n}, z_{\mathrm{M},n})$ of each moving point scatterer $S_{\mathrm{M},n}$ associated with each activity.

|  | Walking | Falling | Sitting |
|---|---|---|---|
| Left ankle | (0.2, 0.15, 0.1) | – | – |
| Right ankle | (0.2, −0.15, 0.1) | – | – |
| Left wrist | (0.2, 0.25, 0.85) | – | – |
| Right wrist | (0.2, −0.25, 0.85) | – | – |
| Waist | (0.2, 0, 1.1) | (4, 0, 1.1) | (4, 0, 1.1) |
| Head | (0.2, 0, 1.75) | (4, 0, 1.75) | (4, 0, 1.75) |

$T_x$ antenna connected to the transmitter station and the other one was an $R_x$ antenna connected to the receiver station. We employed channel number 149 to record the CSI data, i.e., $f_0 = 5.745$ GHz [28]. The bandwidth $B$ was 40 MHz. A B2B connection was used to remove the TV phase distortions, which occur due to the clock asynchronization between the $T_x$ and $R_x$ stations, as shown in Fig. 2 and described in [32]. For realizing the B2B connection, the RF cables 141-MSM+, and RF power splitter ZFSC-2-10G+ with two output and one input ports have been deployed. The input port of the splitter was connected to the $T_x$ station. One of the output ports was connected to a port of the $R_x$ station as a B2B connection, whereas the other port was connected to the $T_x$ antenna. Both of $T_x$ and $R_x$ antennas were collocated at a height of 0.8 m. The source MATLAB code for reading the measured CSI data can be found in [52].

Six IMUs were used to capture motion data simultaneously while collecting the CSI data. Four of the IMUs were from MetaMotionR [53] and the other two were from the Polytechnic School of Engineering of Vilanova i la Geltrú at the Technical University of Catalonia (UPC). A 22-year-old male candidate weighing 76 kg and 1.8 m tall was asked to perform the following activities (see Fig. 2):

- Walking: The candidate stood in front of the $T_x$ and $R_x$ antennas. He wore six IMUs, two on his wrists, two on his ankles, one on his torso, and one on his head. He walked 4 m away from $T_x$ and $R_x$ antennas, and then he stopped.
- Falling: The candidate stood still facing the $T_x$ and $R_x$ antennas at a distance of 4 m. Then, he fell forward on a 15 cm thick mattress. He was wearing two IMUs. One attached to the torso, and the other one was placed on his head.
- Sitting: He stood still facing the $T_x$ and $R_x$ antennas at a distance of 4 m. Then, he sat down on a chair. He was wearing two IMUs at the same locations as those in the falling activity.

The candidate stopped moving for a while after finishing each activity. In the simulation, the location $(x^T, y^T, z^T)$ of $T_x$ and the location $(x^R, y^R, z^R)$ of $R_x$ and were chosen to be $(0, -0.05, 0.8)$ and $(0, 0.05, 0.8)$, respectively. The initial positions $(x_{\mathrm{M},n}, y_{\mathrm{M},n}, z_{\mathrm{M},n})$ of the moving point scatterers are exhibited in Table 1 for each activity.

### B. PROCESSING OF THE COLLECTED DATA

Fig. 3(a) illustrates the steps for processing the recorded CSI data. The collected CSI data were stored in two matrices

**TABLE 2.** The parameters of the used notch filter.

| Name | Value |
|---|---|
| Filter type | Highpass FIR |
| Stopband frequency | 0.1 Hz |
| Passband frequency | 1 Hz |
| Stopband attenuation | 25 dB |
| Passband ripple | 0.01 |
| Design method | Equiripple |

**TABLE 3.** The values of the estimated parameter $a_{M,n}$ of each moving point scatterer $S_{M,n}$ corresponding to each activity.

|  | Walking | Falling | Sitting |
|---|---|---|---|
| Left ankle | 0.150 | – | – |
| Right ankle | 0.138 | – | – |
| Left wrist | 0.086 | – | – |
| Right wrist | 0.105 | – | – |
| Waist | 0.347 | 0.825 | 0.652 |
| Head | 0.174 | 0.175 | 0.348 |

at the $R_x$ station. The first matrix stored the CSI data of the B2B connection, which includes only the TV phase distortions caused the clock asynchronization between the $T_x$ station and the $R_x$ station. The second matrix stored the data representing the desired fading behaviour of the measured channels and the TV phase distortions between the $T_x$ and the $R_x$ stations caused by the clock asynchronization. The second matrix was divided element-wise by the first matrix to get a new third matrix containing the channel transfer function (CTF) $\hat{H}(t, f_q)$, with the desired channel behaviour [54], [55]. Then, the CTF $\hat{H}(t, f_q)$ was summed over the subcarriers to obtain the complex channel gain $\hat{\mu}(t)$

$$\hat{\mu}(t) = \sum_q \hat{H}(t, f_q). \qquad (44)$$

This procedure reduces the background noise of the spectrogram that arises due to measurement imperfections. Because, as mentioned in Section II-C, the bandwidth $B$ is much smaller than the carrier frequency $f_0$, the Doppler frequencies are almost the same for all subcarriers. Hence, the sum in (44) does not have an impact on the micro-Doppler signatures. The zero-value Doppler shifts due to static objects (fixed scatterers) were eliminated by utilizing a notch filter. The parameters of the filter designed in MATLAB can be found in Table 2. Finally, the spectrogram $\hat{S}_q(f, t)$ was computed to reveal the micro-Doppler signature of the candidate's activity.

Fig. 3(b) depicts the block diagram for developing the IMU-driven channel model. The IMU data was recorded simultaneously with the CSI data. The sensors were configured to record accelerations and quaternions simultaneously. Also, the timestamps were recorded and used to synchronize the data. The acceleration data was measured on the local axes of the IMUs. By using the quaternions, the Euler angles and the rotation matrix were constructed to rotate the measured accelerations to the reference frame. The rotated accelerations were numerically integrated first to obtain the TV velocities. The drifts in the obtained TV velocities were removed by using the zero-update (ZUPT) algorithm [56]. The source code of the ZUPT algorithm is available on GitHub [57].

After that, the displacements were determined by integrating the drift-removed velocities.

The spectrogram $\hat{S}_q(f, t)$ and TV-MDS $\hat{B}_{H_q}(t)$ of the measured CSI data were computed first. Then, the TV-MDS $\hat{B}_{H_q}(t)$ was used to compute the contribution of the $n$th moving scatterer $S_{M,n}$ by solving the following mean-square-error (MSE) optimization problem as follows

$$E_{B_{f_q}(t)} = \underset{\substack{a_{M,n} \\ n \in \{1,2,\dots,\mathcal{N}\}}}{\operatorname{argmin}} \int_0^{T_{\text{obs}}} \left( B_{f_q}(t) - \hat{B}_{H_q}(t) \right)^2 dt \qquad (45)$$

where $B_{f_q}(t)$ and $\hat{B}_{H_q}(t)$ were computed by (27) and (42), respectively. After obtaining the contributions of the moving scatterers $a_{M,n}$, TV-CTF $H(t, f_q)$ was generated according to (24). The parameter $\eta$ was set to 2. Finally, the spectrogram $S_q(f, t)$ and the TV-MDS $B_{f_q}(t)$ of $\mu(t)$ were computed. Table 3 shows the estimated values of $a_{M,n}$ associated with each moving point scatterer corresponding to each activity.

### C. DISCUSSION OF THE RESULTS

Figs. 4(a) and 4(b) exhibit the spectrograms $\hat{S}_q(f, t)$ and $S_q(f, t)$ corresponding to the walking activity of the measured CSI and the IMU-driven channel model, respectively. There is a good match between the two spectrograms in Figs. 4(a) and 4(b). The spectrogram of the IMU-driven channel model was computed after the estimation of $a_n$ for $n = 1, 2, \dots, \mathcal{N}$ as in (45). The walking duration took almost 5.5 s, i.e., $T_{\text{obs}} \approx 5.5$ s. The Doppler frequencies have negative values as the candidate was moving away from the $T_x$ and $R_x$ antennas. Thus, the propagation delays $\tau_{M,n}(t)$ and their rate of change $\dot{\tau}_{M,n}(t)$ were increasing. Hence, the Doppler frequencies have negative values according to (17) in Section II-C. The Doppler frequencies corresponding to the head and the torso have the highest power values, unlike the rest of the body segments, as they have the highest body areas. The Doppler shifts caused by the head and torso have ranges from 40 to 50 Hz. The values of the parameter $a_{M,n}$ corresponding to the walking activity are exhibited in Table 3. These values are associated with the

$$S_q^{(c)}(f, t) \approx \frac{2}{\sigma_w \sqrt{\pi}} \Re \left\{ \sum_{n=1}^{\mathcal{N}-1} \sum_{i=n+1}^{\mathcal{N}} X_{M,n,q}(f, t) X_{M,i,q}^*(f, t) + \sum_{m=1}^{\mathcal{M}-1} \sum_{i=m+1}^{\mathcal{M}} X_{F,m} X_{F,i}^* + \sum_{n=1}^{\mathcal{N}} \sum_{i=1}^{\mathcal{M}} X_{M,n,q}(f, t) X_{F,i}^* \right\} \qquad (43)$$
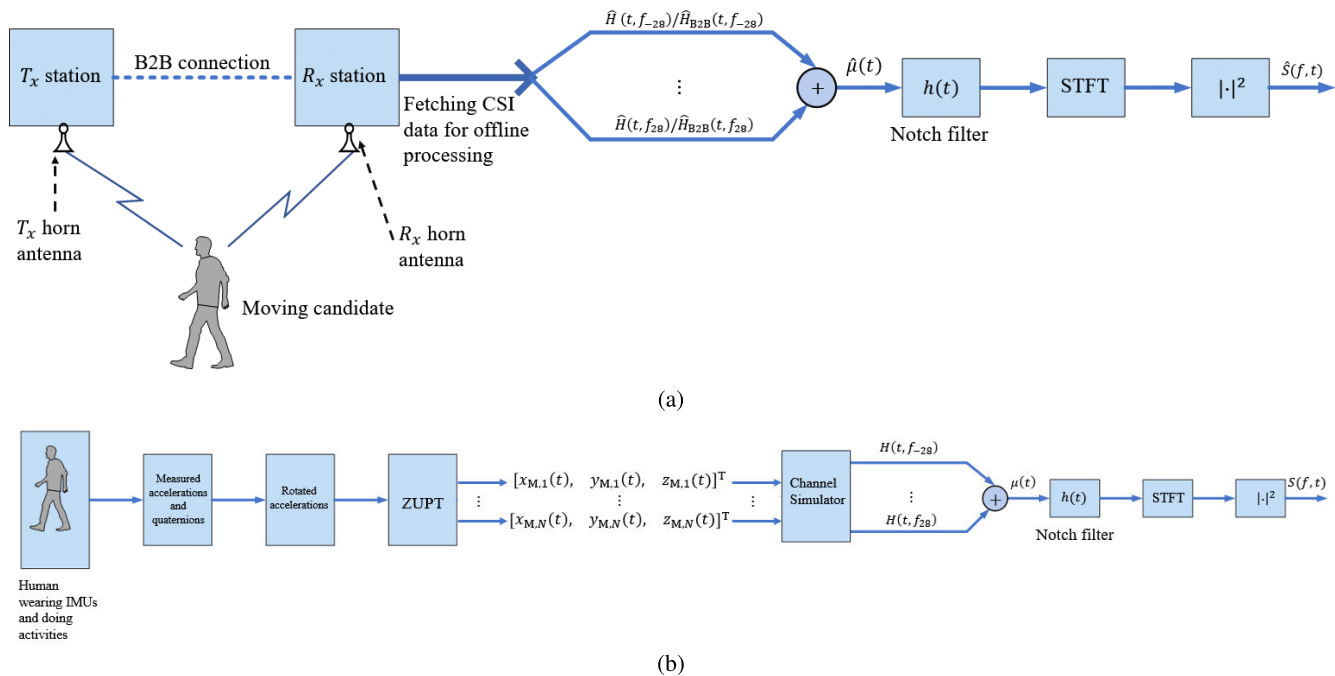
(a)



(b)

**FIGURE 3.** Block diagrams for the (a) CSI data acquisition and processing and (b) IMU-driven channel model.
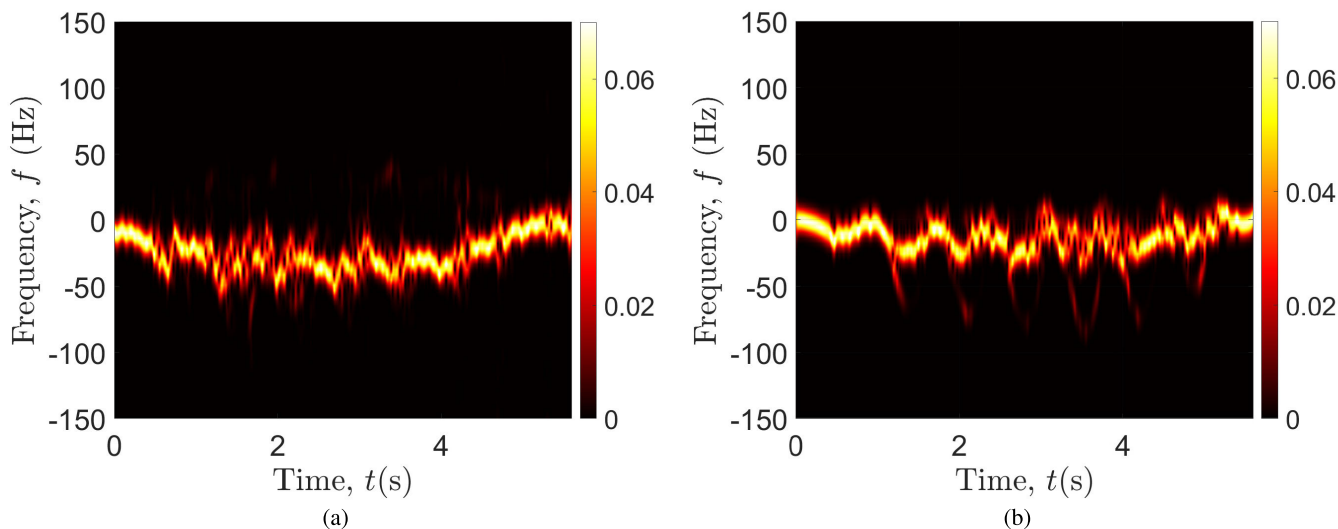


**FIGURE 4.** Walking activity spectrograms $\hat{S}_q(f, t)$ and $S_q(f, t)$ of the (a) measured CSI data and (b) IMU-driven channel model, respectively.

moving scatterers corresponding the left ankle, right ankle, left wrist, right wrist, waist, and head. According to this table, the waist and the head have the highest values, whereas the wrists have the lowest values.

Figs. 5(a) and 5(b) exhibit the analytical solutions of the spectrogram $S_q(f, t)$ and the auto-term $S_q^{(a)}(f, t)$ of the IMU-driven channel model corresponding to the walking activity, respectively. Both of $S_q(f, t)$ and $S_q^{(a)}(f, t)$ were computed by approximating the Doppler frequencies as mentioned in Section III. Although the linear approximations of the Doppler frequencies are obvious in Fig. 5(b), they do not have

a huge impact on the spectrograms as shown in the figures. Furthermore, the Doppler frequency patterns depicted in the figures still provides useful insights in Figs. 5(a) and 5(b) of the walking activity. Note that in Fig. 5(b), the Doppler frequencies corresponding to the moving scatterers are more obvious as there is no cross-term.

The spectrograms $\hat{S}_q(f, t)$ and $S_q(f, t)$ of the measured CSI and the IMU-driven channel model are depicted in Figs. 6(a) and 6(b), respectively. These spectrograms correspond to the falling activity. Surprisingly, there is a good match between $\hat{S}_q(f, t)$ and $S_q(f, t)$, although the candidate
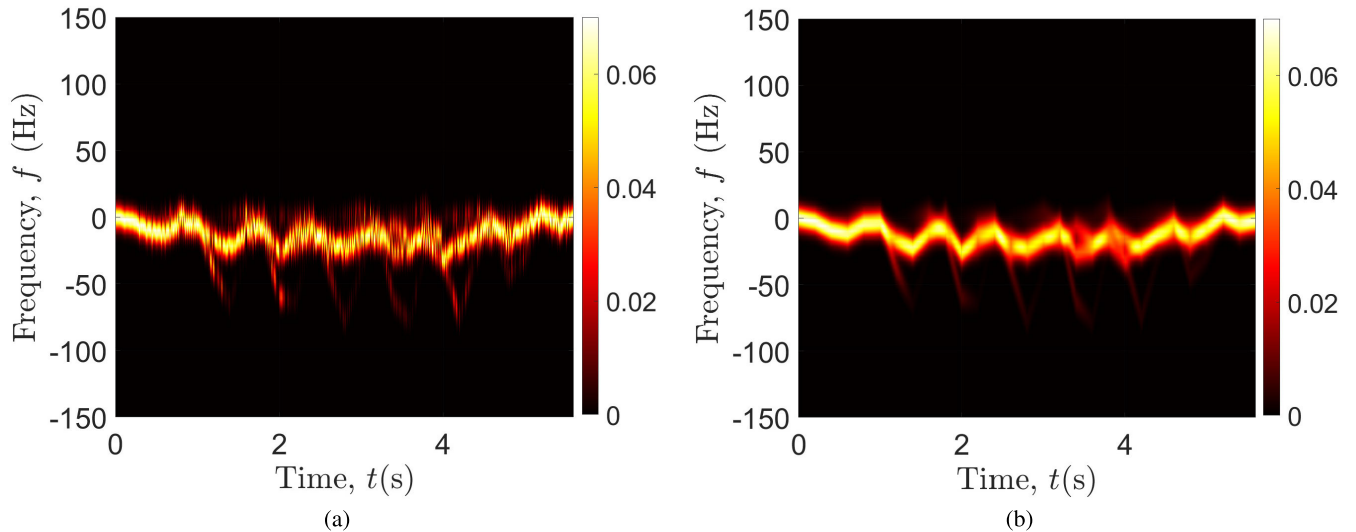
**FIGURE 5.** Approximate analytical solutions of (a) the spectrogram $S_q(f, t)$ and (b) the auto-term $S_q^{(a)}(f, t)$ of the IMU-driven channel model corresponding to the walking scenario.
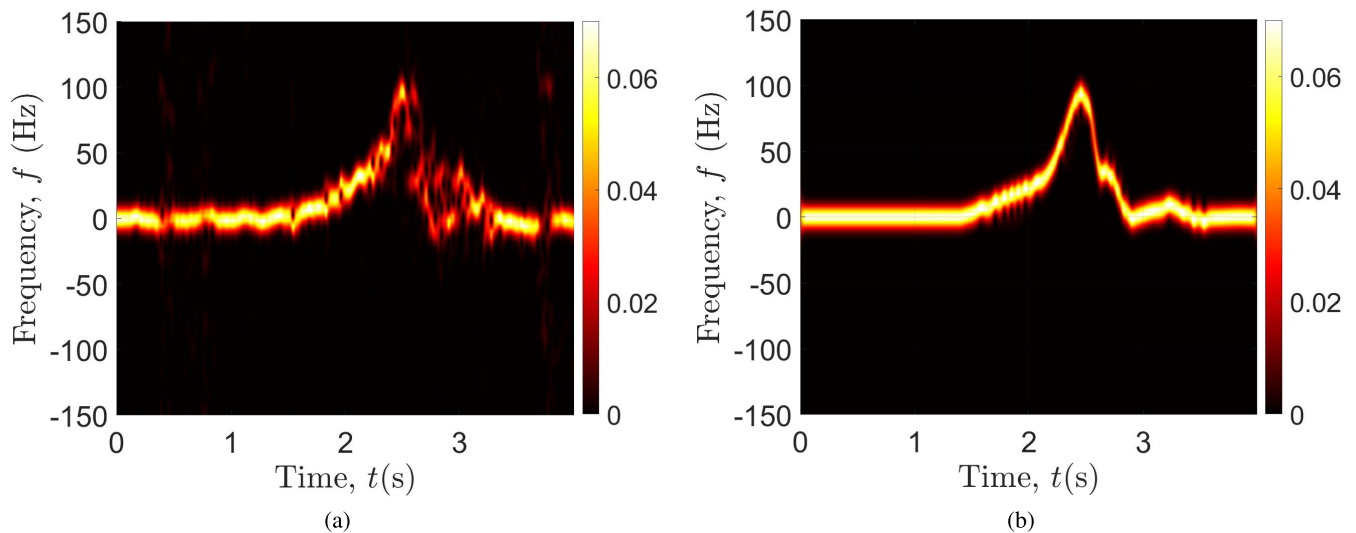


**FIGURE 6.** Falling activity spectrograms $\hat{S}_q(f, t)$ and $S_q(f, t)$ of the (a) measured CSI data and (b) IMU-driven channel model, respectively.

wore two IMUs in this scenario. The falling duration consumed around 1.5 s. The value of the observation interval $T_{\text{obs}}$ was set to 3.5 s when evaluating the parameter computation in (45). The Doppler frequencies had positive values as the candidate was moving towards the $T_x$ and $R_x$ antennas. Thus, the propagation delays $\tau_{\text{M},n}(t)$ were decreasing and their rates of change $\dot{\tau}_{\text{M},n}(t)$ were negative. Hence, the Doppler frequencies had positive values according to (17) in Section II-C. The Doppler frequencies $f_n(t)$ had zero values before time $t \approx 1.5$ s. Then, they increased when the falling started, until they reached a value of 120 Hz approximately at time $t \approx 2.5$ s. At this time $t \approx 2.5$ s, the candidate almost approached the floor. Then, the Doppler frequencies $f_n(t)$ decreased rapidly until they reached zero values in less than 0.5 s. The values of the parameter $a_{\text{M},n}$ corresponding to the falling activity are exhibited in Table 3. These values are

associated with the moving scatterers corresponding the waist and head. According to the table, the waist has a higher value than the head.

Figs. 7(a) and 7(b) demonstrate the analytical solutions of the spectrogram $S_q(f, t)$ and the auto-term $S_q^{(a)}(f, t)$ of the IMU-driven channel model corresponding to the falling activity, respectively. The cross-term in Fig. 7(a) does not have a high impact as the number of the moving scatterers $\mathcal{N}$ is 2 in the falling scenario. By comparing Figs. 7(a) and 7(b) with Fig. 6(b), there are slight degradation of the linear Doppler frequencies at time $t \approx 3$ s. However, the falling patterns are still obvious in Figs. 7(a) and 7(b).

Figs. 8(a) and 8(b) illustrate the spectrograms $\hat{S}_q(f, t)$ and $S_q(f, t)$ corresponding to the sitting activity of the measured CSI data and the IMU-driven channel model, respectively. There is also a good match between $\hat{S}_q(f, t)$ and $S_q(f, t)$. The
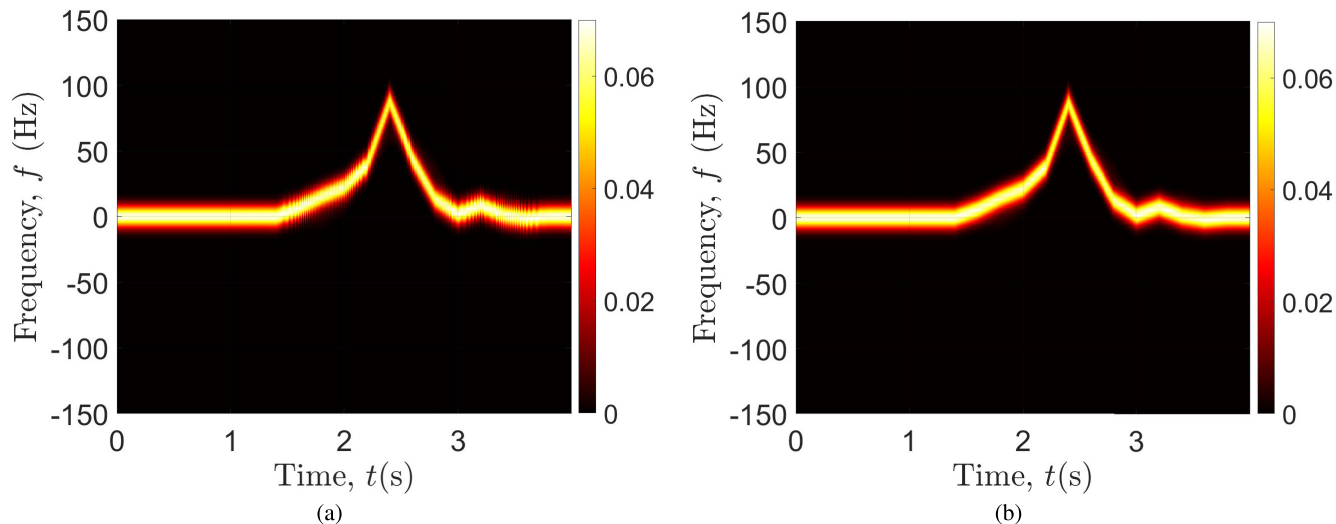
**FIGURE 7.** Approximate analytical solutions of (a) the spectrogram $S_q(f, t)$ and (b) the auto-term $S_q^{(a)}(f, t)$ of the IMU-driven channel model corresponding to the falling scenario.
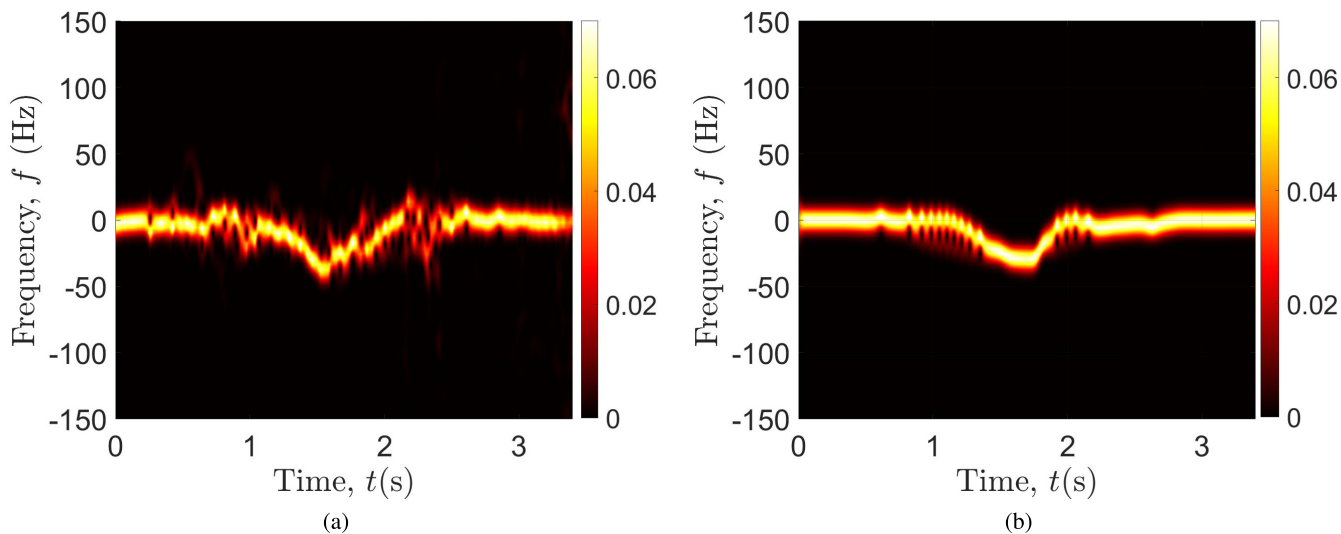


**FIGURE 8.** Sitting activity spectrograms $\hat{S}_q(f, t)$ and $S_q(f, t)$ of the (a) measured CSI data and (b) IMU-driven channel model, respectively.

values of the Doppler frequencies were negative since the candidate was moving away down from the $T_x$ and $R_x$. The value of $T_{\mathrm{obs}}$ was chosen to be 3 s. The sitting duration was 1.5 s; however, the Doppler frequencies $f_n(t)$ reached values of about -50 Hz, unlike those of the falling activity in Figs. 8(a) and 6(b). That is because the candidate's speed during the sitting activity was slower than that of the falling activity. The values of the Doppler frequencies started to decrease at $t \approx 0.5$ s until they reached values of about $-50$ Hz at $t \approx 1.5$ s. Then, they increased slowly until they reached zero values. The values of the parameter $a_{\mathrm{M},n}$ corresponding to the sitting activity and associated with the waist and the head are depicted in Table 3. Again, the waist has a higher value than the head. Figs. 9(a) and 9(b) show the spectrograms $S_q(f, t)$ and $S_q^{(a)}(f, t)$ corresponding to the

sitting activity of the measured CSI data and the IMU-driven channel model, respectively. A slight difference is depicted in Figs. 9(a) and 9(b) due to the linear approximation of the Doppler frequencies; however, the spectrograms still provide insightful results.

Fig. 10(a) depicts the TV-MDSs $\hat{B}_{H_q}(t)$ and $B_{f_q}(t)$ corresponding to the walking activity of the collected CSI data and the IMU-driven channel model, respectively. The TV-MDSs $\hat{B}_{H_q}(t)$ and $B_{f_q}(t)$ in Fig. 10(a) are matching. The TV-MDSs in Fig. 10(a) provide the same trends as those in Figs. 4(a) and 4(b), but with different values. This happens due to the impact of the cross-terms. The TV-MDSs $\hat{B}_{H_q}(t)$ and $B_{f_q}(t)$ corresponding to the falling activity of the measured CSI data and the IMU-driven channel model are exhibited in Fig. 10(b), respectively. There is a good match between
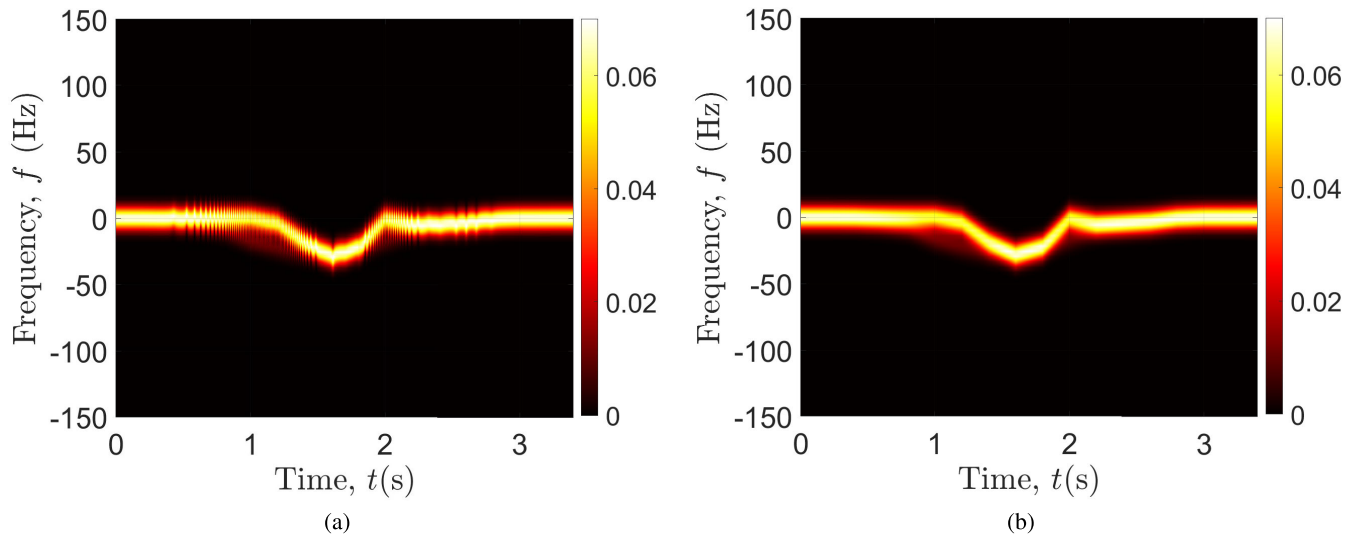
**FIGURE 9.** Approximate analytical solutions of the spectrogram $S_q(f, t)$ and (b) the auto-term $S_q^{(a)}(f, t)$ of the IMU-driven channel model corresponding to the sitting scenario.
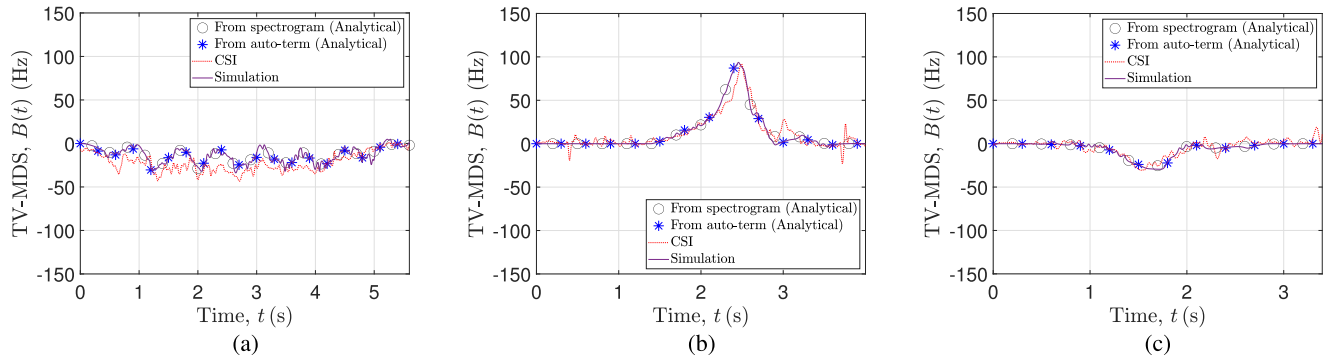


**FIGURE 10.** The TV-MDSs $\hat{B}_{H_q}(t)$ and $B_{f_q}(t)$ of the measured CSI and the IMU-driven channel model, respectively, corresponding to the (a) walking, (b) falling, and (c) sitting activities.

$\hat{B}_{H_q}(t)$ and $B_{f_q}(t)$ in Fig. 10(b). The TV-MDSs in Fig. 10(b) show the same trends as those in Figs. 6(a) and 6(b), but with different values due to the influence of the cross-terms on the TV-MDSs. The TV-MDSs $\hat{B}_{H_q}(t)$ and $B_{f_q}(t)$ of the CSI data and the IMU-driven channel model corresponding to the sitting activity are shown in Fig. 10(c), respectively. A good match is shown between the TV-MDSs $\hat{B}_{H_q}(t)$ and $B_{f_q}(t)$ in Fig. 10(c). The trends of $\hat{B}_{H_q}(t)$ and $B_{f_q}(t)$ in Fig. 10(c) are matching the TV frequency patterns shown in Figs. 8(a) and 8(b); however, they have different values as the cross-terms have influences on $\hat{B}_{H_q}(t)$ and $B_{f_q}(t)$. Note that in Figs. 10(a) and 10(c) the TV-MDSs $B_{f_q}(t)$ computed from the analytical solutions of the spectrogram and the auto-term are still insightful although the Doppler frequencies are linearly approximated.

## V. CONCLUSION

In this paper, we demonstrated the possibility of designing an IMU-driven non-stationary channel model for human activity recognition. Such a model enables the reproducibility of micro-Doppler signatures. We modelled the non-stationary CTF fed with IMU data, TV path gains, and TV Doppler shifts. Furthermore, we explored the micro-Doppler signature of the proposed TV-CTF by means of the spectrogram. We confirmed our proposed model by comparing the micro-Doppler signatures of measured CSI data with a channel model fed with IMU data. Both of the CSI and IMU data were measured simultaneously. The results showed a good match between the micro-Doppler signatures of the IMU-driven channel model and the CSI. For future work, we recommend training fall classifiers with micro-Doppler signatures or the TV-MDSs of the proposed model and test them with measured RF data.

## REFERENCES

[1] (Jun. 2018). *Clinical Trial Transformation Initiative. CTTI Recommendations: Developing Novel Endpoints Generated by Mobile Technology for Use in Clinical Trials.* [Online]. Available: https://www.ctti-clinicaltrials.org/files/novelendpoints-recs.pdf

[2] F. Cerreta, "EMA experience on mHealth technology," in *Proc. PCWP HCPWP Joint Meeting*, Apr. 2018, pp. 1–9.

[3] K. A. Hartholt, R. Lee, E. R. Burns, and E. F. Van Beeck, "Mortality from falls among U.S. Adults aged 75 years or older, 2000–2016," *J. Amer. Med. Assoc.*, vol. 321, no. 21, pp. 2131–2133, Jun. 2019.

[4] *Population Division, World Population Ageing 2020 Highlights (ST/ESA/SER.A/408)*, United Nations, Dept. Econ. Social Affairs, New York, NY, USA, 2020.

[5] E. Warmerdam, J. M. Hausdorff, A. Atrsaei, Y. Zhou, A. Mirelman, K. Aminian, A. J. Espay, C. Hansen, L. J. W. Evers, A. Keller, C. Lamoth, A. Pilotto, L. Rochester, G. Schmidt, B. R. Bloem, and W. Maetzler, "Long-term unsupervised mobility assessment in movement disorders," *Lancet Neurol.*, vol. 19, no. 5, pp. 462–470, May 2020.

[6] M. Babiker, O. O. Khalifa, K. K. Htike, A. Hassan, and M. Zaharadeen, "Automated daily human activity recognition for video surveillance using neural network," in *Proc. IEEE 4th Int. Conf. Smart Instrum., Meas. Appl. (ICSIMA)*, Nov. 2017, pp. 1–5.

[7] K. K. Htike, O. O. Khalifa, H. A. M. Ramli, and M. A. M. Abushariah, "Human activity recognition for video surveillance using sequences of postures," in *Proc. 3rd Int. Conf. e-Technol. Netw. Develop. (ICeND)*, Apr. 2014, pp. 79–82.

[8] W. Lin, M.-T. Sun, R. Poovandran, and Z. Zhang, "Human activity recognition for video surveillance," in *Proc. IEEE Int. Symp. Circuits Syst.*, May 2008, pp. 2737–2740.

[9] S. Park, J. Park, M. Al-Masni, M. Al-Antari, M. Z. Uddin, and T.-S. Kim, "A depth camera-based human activity recognition via deep learning recurrent neural network for health and social care services," *Procedia Comput. Sci.*, vol. 100, pp. 78–84, Jan. 2016.

[10] F. Attal, S. Mohammed, M. Dedabrishvili, F. Chamroukhi, L. Oukhellou, and Y. Amirat, "Physical human activity recognition using wearable sensors," *Sensors*, vol. 15, no. 12, pp. 31314–31338, Dec. 2015.

[11] A. Nandy, J. Saha, C. Chowdhury, and K. P. D. Singh, "Detailed human activity recognition using wearable sensor and smartphones," in *Proc. Int. Conf. Opto-Electron. Appl. Opt. (Optronix)*, Mar. 2019, pp. 1–6.

[12] J. Aggarwal and M. Ryoo, "Human activity analysis: A review," *ACM Comput. Surv.*, vol. 43, no. 3, pp. 1–43, Apr. 2011.

[13] M. Ermes, J. Parkka, and L. Cluitmans, "Advancing from offline to online activity recognition with wearable sensors," in *Proc. 30th Annu. Int. Conf. IEEE Eng. Med. Biol. Soc.*, Aug. 2008, pp. 4451–4454.

[14] Y. He, F. Le Chevalier, and A. G. Yarovoy, "Range-Doppler processing for indoor human tracking by multistatic ultra-wideband radar," in *Proc. 13th Int. Radar Symp.*, May 2012, pp. 250–253.

[15] J. Kwon, S. Lee, and N. Kwak, "Human detection by deep neural networks recognizing micro-Doppler signals of radar," in *Proc. 15th Eur. Radar Conf. (EuRAD)*, Sep. 2018, pp. 198–201.

[16] Y. Kim, S. Ha, and J. Kwon, "Human detection using Doppler radar based on physical characteristics of targets," *IEEE Geosci. Remote Sens. Lett.*, vol. 12, no. 2, pp. 289–293, Feb. 2014.

[17] B. Erol and M. G. Amin, "Radar data cube processing for human activity recognition using multisubspace learning," *IEEE Trans. Aerosp. Electron. Syst.*, vol. 55, no. 6, pp. 3617–3628, Dec. 2019.

[18] B. Jokanović and M. Amin, "Fall detection using deep learning in range-Doppler radars," *IEEE Trans. Aerosp. Electron. Syst.*, vol. 54, no. 1, pp. 180–189, Feb. 2018.

[19] F. Fioranelli, J. Le Kernec, and S. A. Shah, "Radar for health care: Recognizing human activities and monitoring vital signs," *IEEE Potentials*, vol. 38, no. 4, pp. 16–23, Jul. 2019.

[20] Z. Zeng, M. G. Amin, and T. Shan, "Automatic arm motion recognition based on radar micro-Doppler signature envelopes," *IEEE Sensors J.*, vol. 20, no. 22, pp. 13523–13532, Nov. 2020.

[21] M. Ritchie and A. M. Jones, "Micro-Doppler gesture recognition using Doppler, time and range based features," in *Proc. IEEE Radar Conf. (RadarConf)*, Apr. 2019, pp. 1–6.

[22] S. Skaria, A. Al-Hourani, M. Lech, and R. J. Evans, "Hand-gesture recognition using two-antenna Doppler radar with deep convolutional neural networks," *IEEE Sensors J.*, vol. 19, no. 8, pp. 3041–3048, Apr. 2019.

[23] J. Lien, N. Gillian, M. E. Karagozler, P. Amihood, C. Schwesig, E. Olson, H. Raja, and I. Poupyrev, "Soli: Ubiquitous gesture sensing with millimeter wave radar," *ACM Trans. Graph.*, vol. 35, no. 4, pp. 1–19, Jul. 2016.

[24] F. Fioranelli, M. Ritchie, S. Z. Gürbüz, and H. Griffiths, "Feature diversity for optimized human micro-Doppler classification using multistatic radar," *IEEE Trans. Aerosp. Electron. Syst.*, vol. 53, no. 2, pp. 640–654, Apr. 2017.

[25] A.-K. Seifert, A. M. Zoubir, and M. G. Amin, "Detection of gait asymmetry using indoor Doppler radar," in *Proc. IEEE Radar Conf. (RadarConf)*, Apr. 2019, pp. 1–6.

[26] A. K. Seifert, M. G. Amin, and A. M. Zoubir, "Toward unobtrusive in-home gait analysis based on radar micro-Doppler signatures," *IEEE Trans. Biomed. Eng.*, vol. 66, no. 9, pp. 2629–2640, Sep. 2019.

[27] D. Halperin, W. Hu, A. Sheth, and D. Wetherall, "Tool release: Gathering 802.11n traces with channel state information," *ACM SIGCOMM Comput. Commun. Rev.*, vol. 41, no. 1, p. 53, Jan. 2011.

[28] *IEEE Standard for Information Technology—Local and Metropolitan Area Networks—Specific Requirements—Part 11: Wireless LAN Medium Access Control (MAC) and Physical Layer (PHY) Specifications Amendment 5: Enhancements for Higher Throughput*, IEEE Standard 802.11n-2009 (Amendment to IEEE Std 802.11-2007 as amended by IEEE Std 802.11k-2008, IEEE Std 802.11r-2008, IEEE Std 802.11y-2008, and IEEE Std 802.11w-2009), Oct. 2009, pp. 1–565.

[29] Z. Wang, B. Guo, Z. Yu, and X. Zhou, "Wi-Fi CSI-based behavior recognition: From signals and actions to activities," *IEEE Commun. Mag.*, vol. 56, no. 5, pp. 109–115, May 2018.

[30] W. Wang, A. X. Liu, and M. Shahzad, "Gait recognition using WiFi signals," in *Proc. ACM Int. Joint Conf. Pervas. Ubiquitous Comput. (Ubi-Comp)*, New York, NY, USA, 2016, pp. 363–373.

[31] S. Sen, B. Radunovic, R. R. Choudhury, and T. Minka, "You are facing the Mona Lisa: Spot localization using PHY layer information," in *Proc. 10th Int. Conf. Mobile Syst., Appl., Services (MobiSys)*, New York, NY, USA, 2012, pp. 183–196.

[32] N. Keerativoranan, A. Haniz, K. Saito, and J.-I. Takada, "Mitigation of CSI temporal phase rotation with B2B calibration method for fine-grained motion detection analysis on commodity Wi-Fi devices," *Sensors*, vol. 18, no. 11, p. 3795, Nov. 2018.

[33] S. S. Ram, R. Bhalla, and H. Ling, "Simulation of human radar signatures in the presence of ground," in *Proc. IEEE Antennas Propag. Soc. Int. Symp.*, Jun. 2009, pp. 1–4.

[34] J. Park and J. T. Johnson, "Measurements and simulations of multi-frequency human radar signatures," in *Proc. IEEE Int. Symp. Antennas Propag.*, Jul. 2012, pp. 1–2.

[35] P. van Dorp and F. C. A. Groen, "Human walking estimation with radar," *IEE Proc.-Radar, Sonar Navigat.*, vol. 150, no. 5, pp. 356–365, Oct. 2003.

[36] R. Boulic, N. M. Thalmann, and D. Thalmann, "A global human walking model with real-time kinematic personification," *Vis. Comput.*, vol. 6, no. 6, pp. 344–358, Nov. 1990.

[37] C. Karabacak, S. Z. Gurbuz, A. C. Gurbuz, M. B. Guldogan, G. Hendeby, and F. Gustafsson, "Knowledge exploitation for human micro-Doppler classification," *IEEE Geosci. Remote Sens. Lett.*, vol. 12, no. 10, pp. 2125–2129, Oct. 2015.

[38] B. Erol, C. Karabacak, S. Z. Gurbuz, and A. C. Gurbuz, "Simulation of human micro-Doppler signatures with kinect sensor," in *Proc. IEEE Radar Conf.*, May 2014, pp. 0863–0868.

[39] M. Pätzold and C. A. Gutierrez, "Modelling of non-WSSUS channels with time-variant Doppler and delay characteristics," in *Proc. 7th IEEE Int. Conf. Commun. Electron. (ICCE)*, Hue, Vietnam, Jul. 2018, pp. 1–6.

[40] A. Abdelgawwad and M. Päetzold, "A framework for activity monitoring and fall detection based on the characteristics of indoor channels," in *Proc. IEEE 87th Veh. Technol. Conf. (VTC Spring)*, Porto, Portugal, Jun. 2018, pp. 1–7.

[41] H. T. Friis, "A note on a simple transmission formula," *Proc. IRE*, vol. 34, no. 5, pp. 254–256, May 1946.

[42] C. Phillips, D. Sicker, and D. Grunwald, "A survey of wireless path loss prediction and coverage mapping methods," *IEEE Commun. Surveys Tuts.*, vol. 15, no. 1, pp. 255–270, 1st Quart., 2013.

[43] V. Chen, *The Micro-Doppler Effect in Radar* (Artech House Radar Library), 2nd ed. Norwood, MA, USA: Artech House, 2019.

[44] G. L. Stüber, *Principles of Mobile Communications*, 4th ed. Basel, Switzerland: Springer, 2017.

[45] F. Hlawatsch and G. F. Boudreaux-Bartels, "Linear and quadratic time-frequency signal representations," *IEEE Signal Process. Mag.*, vol. 9, no. 2, pp. 21–67, Apr. 1992.

[46] J. B. Allen and L. Rabiner, "A unified approach to short-time Fourier analysis and synthesis," *Proc. IEEE*, vol. 65, no. 11, pp. 1558–1564, Nov. 1977.

[47] B. Boashash, *Time-Frequency Signal Analysis and Processing—A Comprehensive Reference*, 2nd ed. Amsterdam, The Netherlands: Elsevier, 2015.

[48] A. Abdelgawwad and M. Pätzold, "On the influence of walking people on the Doppler spectral characteristics of indoor channels," in *Proc. 28th IEEE Int. Symp. Pers., Indoor Mobile Radio Commun. (PIMRC)*, Montreal, QC, Canada, Oct. 2017, pp. 1–7.

[49] M. Pätzold and C. A. Gutiérrez, "Spectrogram analysis of multipath fading channels under variations of the mobile speed," in *Proc. IEEE 84th Veh. Technol. Conf. (VTC-Fall)*, Montreal, QC, Canada, Sep. 2016, pp. 1–6.

[50] M. Pätzold and C. A. Gutiérrez, "Enhancing the resolution of the spectrogram of non-stationary mobile radio channels by using massive MIMO techniques," in *Proc. IEEE 86th Veh. Technol. Conf. (VTC-Fall)*, Toronto, ON, Canada, Sep. 2017, pp. 1–7.

[51] *Source Code for the CSI Tool*. Accessed: Jul. 21, 2021. [Online]. Available: https://github.com/dhalperi/linux-80211n-csitool/

[52] *Source Code for Processing CSI Data*. Accessed: Jul. 21, 2021. [Online]. Available: https://github.com/dhalperi/linux-80211n-csitool-supplementary

[53] *Sensors for Motion Capture, Biomechanics, Industrial Control, Robotics, Facility Management, Cold Storage, Research, and Product Development*. Accessed: Jul. 21, 2021. [Online]. Available: https://mbientlab.com/

[54] A. Abdelgawwad, A. Borhani, and M. Pätzold, "Modelling, analysis, and simulation of the micro-Doppler effect in wideband indoor channels with confirmation through pendulum experiments," *Sensors*, vol. 20, no. 4, p. 1049, Feb. 2020.

[55] A. Abdelgawwad, A. Catala, and M. Pätzold, "Doppler power characteristics obtained from calibrated channel state information for human activity recognition," in *Proc. IEEE 91st Veh. Technol. Conf. (VTC-Spring)*, May 2020, pp. 1–7.

[56] X. Yun, E. R. Bachmann, H. Moore, and J. Calusdian, "Self-contained position tracking of human movement using small inertial/magnetic sensor modules," in *Proc. IEEE Int. Conf. Robot. Autom.*, Apr. 2007, pp. 2526–2533.

[57] *MATLAB Code for 3D Tracking With IMU*. Accessed: Jul. 21, 2021. [Online]. Available: https://github.com/xioTechnologies/Gait-Tracking-With-x-IMU

**AHMED ABDELGAWWAD** was born in Minya, Egypt, in 1991. He received the bachelor's and master's degrees (Hons.) in information engineering and technology from the German University in Cairo (GUC), in 2013 and 2015, respectively. He is currently pursuing the Ph.D. degree with the University of Agder. His master's degree was related to the complexity reduction of 3D ray-tracing for indoor coverage solutions. His research interests include network modeling and simulation, channel modeling for fall detection systems, non-stationary channel models, and time-frequency analysis for non-stationary channel models.

**ANDREU CATALÀ MALLOFRÉ** received the B.Sc./M.Sc. degree in physics from the University of Barcelona, and the Ph.D. degree from the Technical University of Catalonia (UPC). He is currently a Full Professor with the Department of Automatic Control, UPC. He is also the Director of the Research Centre for Dependency Care and Autonomous Living. He is a coordinator of international and national research projects, among them the European Thematic Network in Falls Prevention Intervention and Security (E-NOFALLS 2013–2016). He is a Spin Off Promoter of SENSE4CARE (http://www.sense4care.com/). His research interests include assistive technologies, artificial intelligence, social robotics, and wearable and intelligent sensors.

**MATTHIAS PÄTZOLD** (Senior Member, IEEE) received the Dipl.-Ing. and Dr.-Ing. degrees in electrical engineering from Ruhr-University Bochum, Bochum, Germany, in 1985 and 1989, respectively. In 1998, he habilitated at the Technical University of Hamburg-Harburg, Hamburg, Germany, in the field of communications engineering. From 1990 to 1992, he worked with ANT Nachrichtentechnik GmbH, Backnang, Germany, on the design and development of digital satellite communication systems. From 1992 to 2001, he was with the Department of Digital Networks, Technical University Hamburg-Harburg. He joined the University of Agder, Grimstad, Norway, in 2001, where he is currently a Full Professor of mobile communications and the Head of the Mobile Communications Group (https://www.mcg.uia.no).

• • •